

pubs.acs.org/JPCC Article

Asymmetrical Spectral Continuum between Anti-Stokes and Stokes Scattering Revealed in Low-Frequency Surface-Enhanced Raman Spectroscopy

Published as part of The Journal of Physical Chemistry virtual special issue "Nanophotonics for Chemical Imaging and Spectroscopy".

Shuo Sun, Dhanusha T. N. Rathnayake, and Yinsheng Guo*



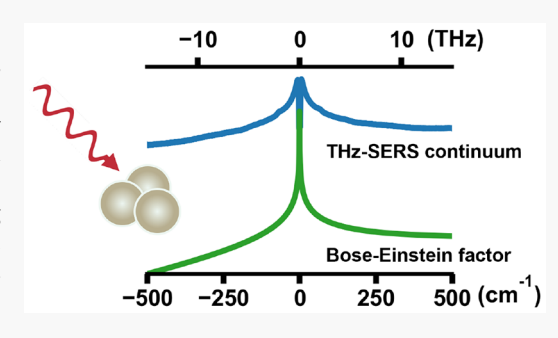
Cite This: J. Phys. Chem. C 2022, 126, 11193-11200



ACCESS I

III Metrics & More

ABSTRACT: An asymmetrical spectral continuum is observed in lowfrequency surface-enhanced Raman spectroscopy (LF-SERS) in the terahertz (THz) region. This background continuum appears as a flat baseline in the Stokes side and a slope in the anti-Stokes side. Analysis shows this asymmetry originates from the different scaling of anti-Stokes and Stokes scattering with respect to the Bose-Einstein distribution. Such asymmetry is readily visible, under room temperature, in the low-frequency THz spectral range. Accounting for this spectral intensity asymmetry reveals the intrinsic continuum background of electronic origin, differing from local normal modes and collective relaxational motions. We also describe a numerical method, independent of line shape models, to determine sample temperatures while



Article Recommendations

simultaneously accounting for this asymmetrical background continuum. Finally, we show that such asymmetrical spectral continuum is generally observable in low-frequency Raman scattering.

INTRODUCTION

Surface-enhanced Raman spectroscopy (SERS) has developed into a major hub for contemporary analytical and physical research.^{1,2} The enhancement of otherwise weak Raman scattering signal enables sensitive detection and identification of chemical and biological analytes, and also provides spectral access to chemical events with exceedingly high temporal or spatial⁴ resolution. Local bond vibrations from molecules of interest have been the focus of most SERS studies. These vibrations reside in the fingerprint region. Their vibrational frequencies allow specific identifications of the chemical components and the systematic frequency shifts have been used to report on the variations of local chemical environments. This in turn enables one to resolve dynamic molecular events temporally or spatially.

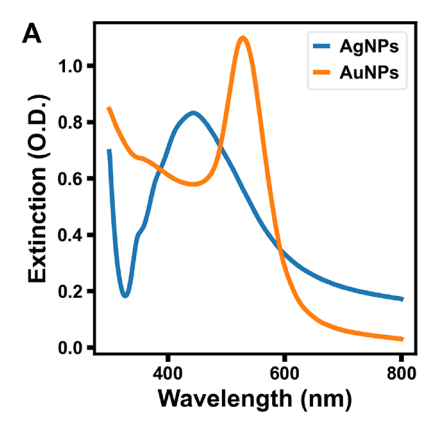
Much of the chemical processes at the molecular level are impacted by rich details of intermolecular interactions involving collective motions and noncovalent secondary bonding. These structural dynamics typically reside in the low frequency, terahertz (THz) region, and often impact or impart functionalities to the materials of interest. For example, THz lattice modes in molecular crystals govern the charge transport in organic optoelectronic materials⁷ and control polymorphic transformations that are important for pharmaceutical formulations.8 Intermolecular interactions and structural dynamics in the THz range in electrolytes underlie the elementary steps of ionic transport. In solid-state semiconductors, THz framework phonons control the dynamic dielectric responses that couple to band edge charge carriers strongly. 10,11

To push the spectral boundary of SERS and to increase the sensitivity limit of monitoring collective structural dynamics, it is desirable to develop low-frequency surface-enhanced Raman spectroscopy in the THz region (LF-SERS or THz-SERS), to combine the technical advantages of both approaches. In our development of the LF-SERS, we have observed a prominent asymmetrical spectral continuum background. The appearance of a broad background continuum has been a topic of sustained interest, especially regarding its relation to the near-field enhancement in SERS. 12,13 The observations of the LF-SERS background continuum have both opened a new spectral window and raised questions on its physical origin and implications. Understanding the origin and implications of this

Received: April 11, 2022 Revised: June 13, 2022 Published: June 28, 2022







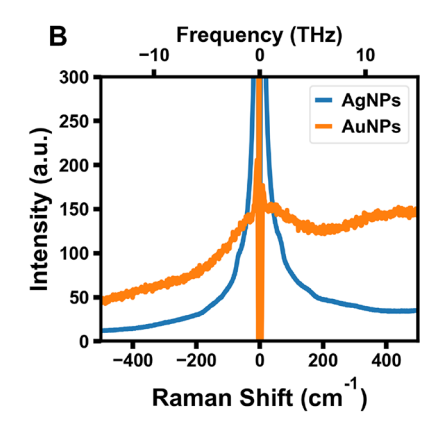


Figure 1. Observations of the asymmetrical spectral continuum in LF-SERS of aggregates of silver nanoparticles (AgNPs) and gold nanoparticles (AuNPs). (A) Solution phase UV—vis extinction spectra of the AgNPs and AuNPs. (B) LF-SERS of dried aggregates of AgNPs and AuNPs. Stokes scattering is plotted using positive wavenumbers to the right. Anti-Stokes scattering is plotted using negative wavenumbers to the left. The sharp dip near 0 cm⁻¹ results from the sharp spectral notch that removes the Rayleigh line.

asymmetrical spectral continuum holds the key to establishing LF-SERS as a new tool for fundamental and analytical investigations in the THz region.

Here we report the observation of an asymmetrical spectral continuum background in LF-SERS and provide an analysis of its origin from the asymmetry in the Bose–Einstein factor. Accounting for this asymmetrical scaling factor reveals the underlying electronic Raman scattering continuum. Our analysis also leads to the recognition of the Bose–Einstein factor as a material-independent signal enhancement mechanism uniquely present in the THz region. The explicit asymmetry in the Bose–Einstein factor can be utilized to yield local temperature information from a spectral continuum, in place of the Boltzmann factor scaled peak intensity ratio. The explicit asymmetry can also be leveraged to distinguish signal photons of different origins. Furthermore, we show that our analysis has broader applications in understanding the spectral background of bulk materials.

METHODS

Synthesis of Colloidal Au Nanoparticles. Turkevich's method 14,15 was used to reduce gold chloride (gold chloride trihydrate, Sigma-Aldrich) with sodium citrate (Sigma-Aldrich) in an aqueous solution. A volume of 50 mL of 0.00025 M HAuCl₄·3H₂O solution was heated to boil and a volume of about 0.5 mL of 0.034 M sodium citrate solution was added. After approximately 5 min, colloidal gold nanoparticles were formed. The volume of sodium citrate solution was used to tune the size of the product gold nanoparticles.

Synthesis of Colloidal Ag Nanoparticles. A modified Turkevich's method was used to reduce silver nitrate with sodium citrate aqueous solution. A volume of 25 mL of 0.005 M silver nitrate solution was diluted to 125 mL and heated to a boil under stirring. Then a volume of 5 mL of 1% sodium citrate was added. Heating and stirring continued until the solution color change was evident. Subsequently, the heating was stopped, and the solution was allowed to rest to cool down to room temperature.

Low-Frequency Surface-Enhanced Raman Spectroscopy. These studies were carried out using home-built confocal micro-Raman setups.

Raman excitation at 532 nm is provided by a single frequency laser (Coherent Verdi V2). The excitation laser is coupled into a home-built microscope using the band-pass

filter of a volume Bragg grating filter set (OptiGrate, 532 nm). The excitation laser is focused on the sample surface using a microscope objective and the Raman signal is collected in the backscattering geometry using the same objective. A Nikon 60× 0.7 NA objective was used to collect Raman spectra from AgNPs, AuNPs, and bulk gold. A Nikon 20× 0.45 NA objective was used to collect Raman spectra from the sapphire. The volume Bragg grating band-pass filter also serves as a dichroic to reject the laser line from entering into the detection path. Three volume Bragg grating notch filters follow the bandpass filter to suppress the laser line with a full width at half-maximum optical density at about 7 cm⁻¹ above and below 0 cm⁻¹. The filtered signal is sent into a spectrometer (IsoPlane-320), dispersed by a 1800 grooves/mm grating, and captured by a thermoelectrically cooled CCD (PIXIS-BRX400).

Raman excitation at 830 nm is provided by a volume holographic grating stabilized diode laser module (Ondax), preassembled with the volume holographic grating notch filter module. The excitation laser is coupled into the same homebuilt microscope and focused on the sample using a microscope objective. The retro-reflected light is sent back into the volume holographic grating filter module, after which coupled into the spectrometer using a multimode optical fiber. The filtered signal is dispersed by a 1200 grooves/mm grating, and the spectra are captured by the thermoelectrically cooled CCD.

■ RESULTS AND DISCUSSION

Figure 1 shows our observation of the asymmetrical spectral continuum background in low frequency surface-enhanced Raman spectroscopy. Colloidal gold and silver nanoparticle assemblies (AuNPs and AgNPs), common substrates for standard SERS measurements, were synthesized following a modified Turkevich method. The solution phase optical extinction spectra of the colloidal nanoparticles are shown in Figure 1A. The nanoparticles were then drop-casted onto silicon wafer substrates. It is worth noting that once aggregated, plasmonic resonances from individual particles couple with each other and both their near-field response and far-field scattering spectra change consequently. Furthermore, the frequency dependence of near-field enhancement differs from the far-field observable dark-field scattering spectra. The LF-SERS spectra were measured from AuNPs and AgNPs using 532 nm excitation with volume Bragg grating filters and

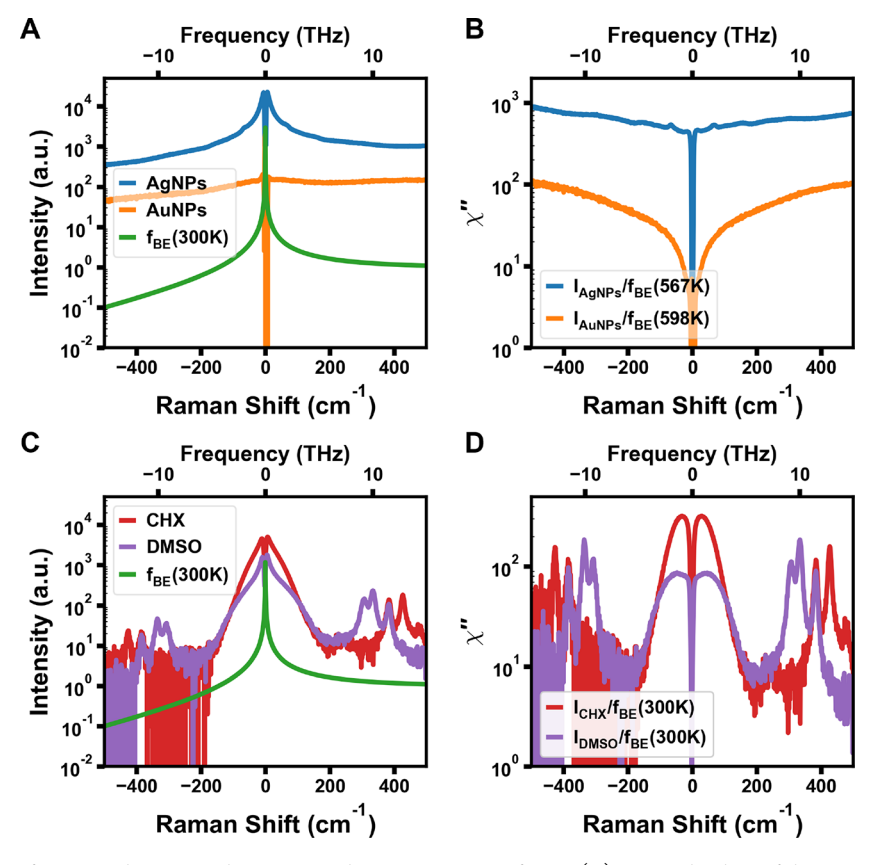


Figure 2. LF-SERS spectra after normalization with respect to the Bose–Einstein factor. (A) Log scale plots of the LF-SERS spectra of AgNPs and AuNPs and the Bose–Einstein factor, showing the correspondence between the spectral continuum background and frequency-dependent magnitude of the Bose–Einstein factor. (B) LF-SERS spectra of AgNPs and AuNPs after normalization with respect to the Bose–Einstein factor at the optimal temperatures accounting for the asymmetry, AgNPs at 567 K and AuNPs at 598 K. (C) Log scale plots of the LF Raman spectra of cyclohexane (CHX) and dimethyl sulfoxide (DMSO) and the Bose–Einstein factor at 300 K. (D) LFR spectra of CHX and DMSO normalized with respect to the Bose–Einstein factor at 300 K.

the results are shown in Figure 1B. In both cases, we observed a spectral continuum background, whose intensity decreases as the probe frequency moves away from the Rayleigh line. The spectral background is asymmetrical in that its intensity approaches zero in the anti-Stokes scattering and converge to a finite constant value in the Stokes scattering.

To explore the physical origin of such spectral asymmetry, we first examine factors that impact the Raman scattering intensity. For a general Raman process, the scattering intensity scales with a thermal population factor f_{BE} , and the intrinsic Raman susceptibility χ'' , where $\chi = \chi' + \chi''$ with χ'' being the Raman resonant part of the full susceptibility. This is described in eq 1.¹⁷

For a typical first-order Raman process, the thermal population factor f_{BE} is expressed as eq 2, which is largely determined by the Bose–Einstein distribution n_{BE} as defined in eq 3. Hence, we refer to f_{BE} as the Bose–Einstein factor. It should be noted that this Bose–Einstein factor differs between the Stokes and anti-Stokes scattering by the +1 term. The physical origin of this asymmetrical +1 term in f_{BE} can be described as follows. In anti-Stokes scattering, a vibrational excitation in the material is annihilated and transfers its energy to the scattered light, producing a blue-shifted photon. The probability of the anti-Stokes scattering process is proportional to the available population of the vibrational excited state. In Stokes scattering, energy is transferred from the incident light to the material and a vibrational excitation is created,

producing a red-shifted scattered photon. The Stokes scattering process can always occur regardless of the available vibrational population.

$$I \propto f_{BE} \chi''$$
 (1)

$$f_{BE} = \begin{cases} n_{BE} + 1 & \text{(Stokes scattering)} \\ n_{BE} & \text{(anti-Stokes scattering)} \end{cases}$$
 (2)

$$n_{BE}(\omega, T) = \frac{1}{\exp\left(\frac{\hbar\omega}{k_{\rm B}T}\right) - 1}$$
(3)

Next we explore the spectral implications of the asymmetrical +1 term in the Bose–Einstein factor. The Bose–Einstein factor is plotted along with observed LF-SERS spectra in Figure 2A. The asymmetrical +1 term in the Bose–Einstein factor produces an asymmetrical frequency-dependent intensity profile, which correlates with the observed asymmetrical spectral continuum. Such asymmetry is intrinsic to all Raman processes that originate from excitations that follow the Bose–Einstein statistics.¹⁸

One common manifestation of the Bose–Einstein factor in conventional Raman measurements ($\nu > 200~{\rm cm}^{-1}$ or fingerprint region) is that the anti-Stokes scattering intensity significantly weakens as the vibrational frequency increases. This behavior is not usually considered as noteworthy since often Stokes scattering of discrete modes from local bond

vibrations are of interest mainly for chemical analysis purposes. In the fingerprint spectral region, n_BE is small and the Bose–Einstein factor f_{BE} becomes essentially a unity factor. However, in the low frequency THz region, spectral continuum features arise in various solids and liquids often when the damping is strong or the restoration forces are weak. ^{9,10} In the presence of an underlying spectral continuum, the asymmetry in the Bose–Einstein factor becomes prominent and visible in the Raman scattering in the low frequency THz spectral range.

Accounting for the asymmetrical scaling with respect to the Bose-Einstein factor symmetrizes the anti-Stokes and Stokes sides and reveals the underlying intrinsic spectral features. Figure 2B shows the susceptibility representation of THz-SERS from AgNPs and AuNPs after normalization with respect to the Bose-Einstein factor under optimal temperature (temperature optimization discussed later). To understand the normalized spectra, we compare and contrast them with well-known model systems that also exhibit spectral continuum in the THz region. We measured the Raman scattering from dimethyl sulfoxide and cyclohexane, examples of typical polar and nonpolar liquids, respectively. Parts C and D of Figure 2 show their Raman scattering intensity before and after the normalization with respect to the optimal Bose-Einstein factor. The spectral continuum from the liquids results from relaxational motions of their molecules.^{9,19}

The THz-SERS continuum and the relaxational continuum have several distinctions in the following aspects. First, their frequency dependence is qualitatively different. The molecular liquid relaxational continuum has a pronounced frequency dependence, whose intensity decreases rapidly as frequency increases beyond the THz region. The THz-SERS continuum, on the other hand, shows relatively weaker and opposite frequency dependence. That is, the THz-SERS continuum intensity slowly increases as frequency increases. Second, the baseline intensity levels of the two types of continua differ by orders of magnitude. The baseline intensities are proportional to the actual number of signal photons collected in the measurements. The baseline level of the molecular liquid relaxational continuum is virtually zero. The baseline of the THz-SERS continuum is of finite intensity and orders of magnitude higher than that of the relaxational continuum. Third, the optimal temperatures, at which the spectra become symmetrized, are drastically different between the THz-SERS continuum and the molecular liquid relaxational continuum. For both molecular liquids and colloidal nanoparticles, Raman measurements were done under ambient conditions using the same excitation wavelength at 532 nm and similar excitation power at a few milliwatts. For the THz-SERS continuum, the optimal temperatures fall between 500 and 600 K. For the relaxational continuum, however, the optimal temperatures match well with room temperature at about 300 K.

All three characteristic differences suggest that the relaxational continuum and THz-SERS continuum are produced by qualitatively different mechanisms. Anharmonic motions with little or no restoration forces often produce spectral continuum features that extend toward zero frequency. Relaxational motions in liquids are prototypical examples of such processes. The relaxational dynamics are also present in solid-state materials such as polymers and other dielectrics. These relaxations exhibit pronounced frequency dependence well described by a variety of dielectric models, among which the Debye relaxation is one of the simplest. On the other hand, AgNPs and AuNPs support plasmonic and electronic

resonances at the excitation wavelength. The high baseline level and its weak frequency dependence indicate an electronic Raman scattering origin for the THz-SERS continuum. The high temperature inferred from the THz-SERS continuum is consistent with the strong resonance, finite losses, and limited interfacial thermal conductivities of the nanoparticle aggregates. ^{23,24}

After recognizing the strong contribution of electronic Raman scattering component, we compare the THz-SERS continuum between AgNPs and AuNPs. In AgNPs, discrete peaks were observed around 67 cm⁻¹ with a narrow line width, which indicates vibrational features overlaid on top of the electronic Raman scattering background. In AuNPs, no such spectrally sharp feature was visible, and the continuum background dominates. In addition, AgNPs exhibit significantly stronger and flatter background continuum than that of the AuNPs. These spectral differences originate from the electronic structures of silver and gold. AgNPs have good localized surface plasmon response with low losses at the excitation wavelength of 532 nm or 2.33 eV, well described by a Drude response.²⁵ For AuNPs, however, their optical response to excitation light is largely determined by interband transitions from the filled d bands to the partially filled sp band. 26 As a result the optical response of AuNPs become lossier at the excitation wavelength.

Accounting for the Bose-Einstein factor with the asymmetrical +1 term inherently distinguishes the Bosonic from non-Bosonic signals. By the term Bosonic, we refer to physical processes that obey the Bose-Einstein distribution, such as molecular bond vibrations, optical and acoustical phonons in a crystalline lattice, relaxational motions in liquids, etc. It is worth noting that elementary excitations of an electron gas and plasmons can also be described as a harmonic oscillator and thus follow the Bose–Einstein scaling factor as well. ^{17,18} In an inelastic light scattering experiment, signals from these processes all scale with the asymmetrical Bose-Einstein factor, namely $I_S \propto n + 1$ for Stokes scattering and $I_{AS} \propto n$ for anti-Stokes scattering in first-order processes. Non-Bosonic signals, however, do not originate from these processes and are not scaled by the Bose-Einstein factor. Photoluminescence background is a prototypical example of a non-Bosonic signal with distinct physical origin. In practice, both types of signal photons, if present, are collected together. It is difficult to distinguish them without additional information such as spectral line width or polarization. Understanding the nature of the SERS background has been a topic of continued interest.²

The existence of non-Bosonic processes within the observed spectral continuum can be readily revealed by its different scaling behavior through the normalization of the Bose-Einstein factor. The THz-SERS spectra, shown in Figure 2, exhibit asymmetrical spectral continuum backgrounds in the low frequency region for both colloidal AuNPs and AgNPs. After the normalization of the Bose-Einstein factor, the AgNP spectrum shows virtually flat baseline with broad bands, which indicates that the observed continuum originates from bosonic processes and has been fully accounted for. The normalized AuNP LF-SERS spectrum, however, shows a baseline that drastically decreases when approaching the Rayleigh line. Numerically, this behavior results from dividing a flat (or slowly varying) spectral response by the diverging Bose-Einstein factor as $\hbar\omega$ approaches zero. Physically, this behavior is indicative of the existence of a spectrally smooth, non-

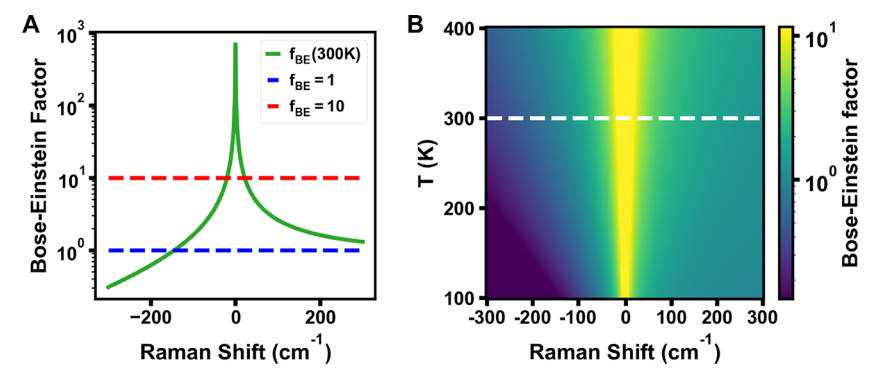


Figure 3. Bose–Einstein factor in Stokes and anti-Stokes Raman scattering. (A) Line plot of the Bose–Einstein factor at 300 K over the THz region. Horizontal dashed lines show $f_{BE} > 1$ in the THz region resulting in signal enhancement compared with the fingerprint region. (B) 2D colorplot of the Bose–Einstein factor over temperature and frequency, showing the asymmetry between anti-Stokes and Stokes processes. The white dashed line corresponds to the line plot in part A.

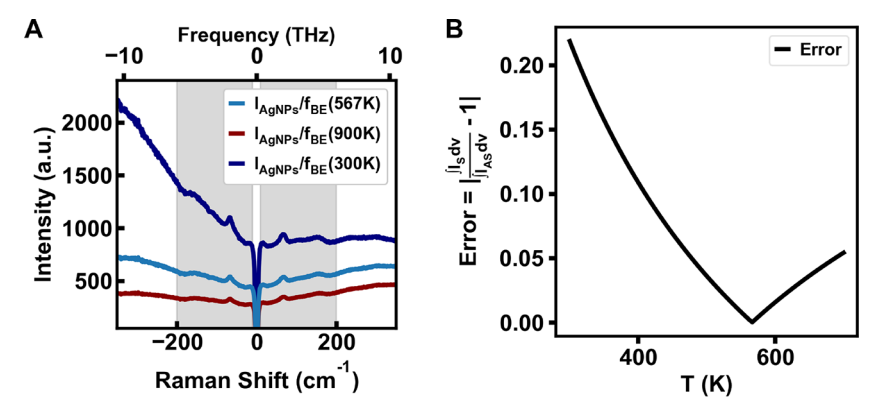


Figure 4. Temperature determination via a one-parameter optimization process leveraging the asymmetry of the Bose–Einstein factor between Stokes and anti-Stokes Raman scattering. (A) low frequency Raman scattering from AgNPs scaled by the Bose–Einstein factor at high (900 K), optimal (567 K), and low (300 K) temperatures. (B) Error function for the optimization process reaching its only global minimum point when anti-Stokes and Stokes spectra are symmetrized. The error function is always positive and minimizes toward zero.

Bosonic component in the collected signals. Our data suggest the electronic interband transitions in AuNPs introduce losses to the optical response and produce signal photons of non-Bosonic origin. The existence of such a non-Bosonic component is difficult to distinguish otherwise, but is readily revealed through the analysis using the Bose–Einstein factor leveraging its asymmetry from the +1 term.

In addition to spectral symmetrization and distinction of signal origins, the Bose-Einstein factor can be viewed as a signal enhancement mechanism inherently available in the low frequency THz region. Parts A and B of Figure 3 plot the Bose–Einstein factor as a function of ω and T. At T = 300 K, the Bose-Einstein factor becomes greater than 2 for the spectral region below 140 cm⁻¹, and greater than 10 for the spectral region below 20 cm⁻¹, as shown in Figure 3A. The magnitude and asymmetry of the Bose-Einstein factor over broad ranges of ω and T are shown in Figure 3B. The Raman scattering process generally has low cross sections compared with other forms of spectroscopy such as photoluminescence. Over the past few decades, various enhancement mechanisms have been identified and studied, 1,28 such as resonance with electronic transitions of molecules and materials, 29,30 plasmonic response of noble metal nanoparticles, 28 chemical enhancement via molecular charge transfer,³¹ as well as optical interferences. 32,33 Here we note that the Bose-Einstein factor comprises a universal signal enhancement mechanism for Raman scattering uniquely significant in the THz spectral

region. Although of limited magnitude compared with other enhancement mechanisms listed above, this enhancement factor is independent of materials properties and substrate structure, and depends only on temperature and frequency as dictated by eq 3.

We now turn to the determination of the optimal temperatures used in the previous discussion. Our analysis of the Bose-Einstein factor in Raman scattering provides a single-variable method of temperature measurement, independent of spectral line shape models. This temperature measurement process is demonstrated in Figure 4. In this method, a spectral region between ω_1 and ω_2 is first selected for analysis. The signal intensities measured over the selected spectral region, proportional to signal photons emitted, will be first scaled by the Bose-Einstein factor using temperature as its input parameter, and then numerically integrated. When the input parameter T matches with the sample temperature, the anti-Stokes side integral becomes equal to the Stokes side integral. The difference between the integrals of the two sides then serves as the error function for the optimization procedure, and can be written as eq 4. Figure 4A shows a LF-SERS spectrum scaled by the Bose-Einstein factor at a range of temperature values. After normalization by the Bose-Einstein factor, the anti-Stokes intensity will be scaled to be higher than the Stokes side, if the input temperature is too low (300 K). Conversely, the Stokes side will be emphasized more than the anti-Stokes side, if the input temperature is too high

(900 K). The two sides become symmetrical only when the input temperature matches the physical temperature of the sample, which minimizes the value of the error function (567 K). The trajectory of an example of this numerical optimization process is shown in Figure 4B, showing a single minimal point that guarantees easy convergence. This Bose–Einstein normalization method formulates temperature measurement in Raman spectroscopy into a single-variable numerical optimization problem that does not make any assumption of the spectral lineshapes.

$$\arg\min_{T>0} Error(T; \omega_1, \omega_2) = \left| \frac{\int_{\omega_1}^{\omega_2} \frac{I_s(\omega)}{n_{BE}(\omega; T) + 1} d\omega}{\int_{\omega_1}^{\omega_2} \frac{I_{AS}(\omega)}{n_{BE}(\omega; T)} d\omega} - 1 \right|$$
(4)

A common practice to determine temperature in Raman spectroscopy is to fit the anti-Stokes/Stokes peak pair of the chosen Raman mode and calculate temperature based the intensity ratio. The ratio relates to the effective temperature following eq 5, where C is a numerical factor accounting for intrinsic and instrumental wavelength dependencies. 30,34 This peak pair intensity ratio method requires the presence of individual discrete Raman mode well described by standard spectral line shape models. In our Bose-Einstein factorization method, if one chooses the integration interval to cover an individual discrete Raman mode, it reduces back to be the equivalent of the peak pair intensity ratio method, but without the need to fit the spectral line shape. When no well-defined peak is observable, the intensity ratio method is not directly applicable, whereas the Bose-Einstein factorization method can still be straightforwardly applied. Since the Bose-Einstein factor is independent of spectral line shape models, it has the advantage over the peak intensity ratio method in that the Bose-Einstein factorization method handles spectral continuum, ill-defined broad peaks, and dense peak groups equally

$$\frac{I_{anti-Stokes}}{I_{Stokes}} = C \frac{n}{n+1} = C \exp\left(-\frac{\hbar\omega}{k_{\rm B}T}\right)$$
 (5)

Finally, we show that a similar asymmetrical spectral continuum can also be observed in other bulk systems beyond colloidal AuNPs. Figure 5 shows that the low frequency Raman scattering from bulk gold metal surface displays an asymmetrical continuum background that follows the Bose-Einstein factor. For bulk gold, electronic processes similar to the AuNPs case are responsible for producing this continuum background. The spectral line shape differs between the bulk and nanoparticle cases likely due to the additional confinement in AuNPs that renders more electronic states optically accessible. Furthermore, the asymmetrical continuum background is also observable from crystalline dielectric materials, for example from sapphire substrates shown in Figure 5. The cluster of densely spaced low-frequency modes in the sapphire Raman spectrum originate from molecular rotations from the air. The rotational modes from air serve as a qualitative internal reference on the magnitude of Raman scattering cross sections. These air rotational modes, present in the sapphire spectrum and invisible in the gold spectrum, indicate the Raman scattering cross sections of sapphire Raman features are small. As discussed above, the appearance of spectral background tracking the asymmetry of the Bose-Einstein factor indicates

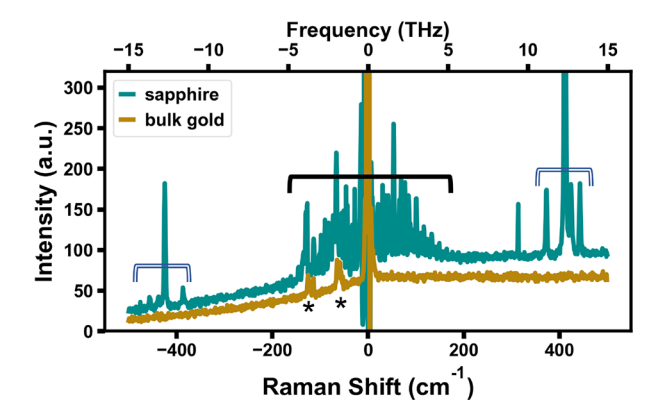


Figure 5. Observations of the Bose—Einstein asymmetrical spectral continuum in bulk dielectric sapphire and bulk metal gold. Asterisk: spectral artifact due to ghost reflections from a strong Rayleigh line. Region under solid black bracket contains rotational modes from the air. Region under the double blue line bracket contains phonon modes of sapphire. Both show flat spectral continuum background tracking the asymmetry of the Bose—Einstein factor.

the existence of an underlying spectrally smooth continuum response. For bulk sapphire, however, the exact nature of the underlying spectral continuum is not clear and will be the subject of future investigations. We note that parasitic photoluminescence processes have been observed in sapphires used in solid-state lighting applications under intensive illumination.³⁵ Optically active electronic states exist in undoped sapphire originating possibly from lattice defects and produce broadband emissions.³⁶

CONCLUSIONS

In summary, we have observed the appearance of an asymmetrical spectral continuum background in the THz-SERS of AuNPs and AgNPs. The asymmetrical spectral continuum originates from the intrinsic asymmetry of the Bose-Einstein factor that scales the Stokes $(n_{BE} + 1)$ and anti-Stokes (n_{BE}) scattering intensities differently. After accounting for the Bose-Einstein factor, one obtains the underlying broad symmetrical THz-SERS continuum, having electronic origins and showing a weak frequency dependence. The asymmetry in the Bose-Einstein factor can be leveraged to distinguish signal photons of Bosonic and non-Bosonic origins. The Bose-Einstein factor can be viewed as a universal Raman enhancement mechanism in the THz region that is distinct from, and independent of, molecular and plasmonic resonances. We have utilized the asymmetry in the Bose-Einstein factor to formulate Raman thermometry into a singlevariable optimization problem. This allows one to implement a simple and effective numerical method for temperature measurement via Raman spectroscopy that is independent of spectral line shape models and handles spectral continuum well. Finally, we note the asymmetrical spectral continuum background exists beyond colloidal plasmonic systems and appears in solid dielectric and metallic materials, broadening the useful scope of our analysis.

AUTHOR INFORMATION

Corresponding Author

Yinsheng Guo – Department of Chemistry, University of Nebraska—Lincoln, Lincoln, Nebraska 68526, United States; orcid.org/0000-0002-0571-8447; Email: yinshengguo@unl.edu

Authors

Shuo Sun – Department of Chemistry, University of Nebraska—Lincoln, Lincoln, Nebraska 68526, United States

Dhanusha T. N. Rathnayake – Department of Chemistry, University of Nebraska—Lincoln, Lincoln, Nebraska 68526, United States

Complete contact information is available at: https://pubs.acs.org/10.1021/acs.jpcc.2c02486

Notes

The authors declare no competing financial interest.

ACKNOWLEDGMENTS

This work is supported by the National Science Foundation/EPSCoR RII Track-1: Emergent Quantum Materials and Technologies (EQUATE), Award OIA-2044049. D.T.N.R. acknowledges support from the Nebraska Public Power District through the Nebraska Center for Energy Sciences Research at the University of Nebraska-Lincoln. Y.G. thanks Prof. Craig Eckhardt for help with experimental resources and scientific discussions.

REFERENCES

- (1) Le Ru, E. C.; Etchegoin, P. G. In *Principles of Surface-Enhanced Raman Spectroscopy*; Le Ru, E. C., Etchegoin, P. G., Eds.; Elsevier: Amsterdam, 2009.
- (2) Langer, J.; et al. Present and Future of Surface-Enhanced Raman Scattering. ACS Nano 2020, 14, 28-117.
- (3) Gruenke, N. L.; Cardinal, M. F.; McAnally, M. O.; Frontiera, R. R.; Schatz, G. C.; Van Duyne, R. P. Ultrafast and Nonlinear Surface-Enhanced Raman Spectroscopy. *Chem. Soc. Rev.* **2016**, *45*, 2263–2290.
- (4) Mahapatra, S.; Li, L.; Schultz, J. F.; Jiang, N. Tip-Enhanced Raman Spectroscopy: Chemical Analysis with Nanoscale to Angstrom Scale Resolution. *J. Chem. Phys.* **2020**, *153*, 010902.
- (5) Henry, A.-I.; Ueltschi, T. W.; McAnally, M. O.; Van Duyne, R. P. Spiers Memorial Lecture. *Faraday Discuss.* **2017**, 205, 9–30.
- (6) Yu, Z.; Frontiera, R. R. Intermolecular Forces Dictate Vibrational Energy Transfer in Plasmonic–Molecule Systems. *ACS Nano* **2022**, *16*, 847–854.
- (7) Salzillo, T.; Brillante, A.; Girlando, A. Terahertz Raman Scattering as a Probe for Electron—Phonon Coupling, Disorder and Correlation Length in Molecular Materials. *J. Mater. Chem. C* **2021**, 9, 10677—10688.
- (8) Chang, C.-F.; Wang, S.-C.; Shigeto, S. In Situ Ultralow-Frequency Raman Tracking of the Polymorphic Transformation of Crystalline 1,1'-Binaphthyl. J. Phys. Chem. C 2014, 118, 2702–2709.
- (9) Paschoal, V. H.; Faria, L. F. O.; Ribeiro, M. C. C. Vibrational Spectroscopy of Ionic Liquids. *Chem. Rev.* **2017**, *117*, 7053–7112.
- (10) Yaffe, O.; Guo, Y.; Tan, L. Z.; Egger, D. A.; Hull, T.; Stoumpos, C. C.; Zheng, F.; Heinz, T. F.; Kronik, L.; Kanatzidis, M. G.; et al. Local Polar Fluctuations in Lead Halide Perovskite Crystals. *Phys. Rev. Lett.* **2017**, *118*, 136001.
- (11) Guo, Y.; Yaffe, O.; Hull, T. D.; Owen, J. S.; Reichman, D. R.; Brus, L. E. Dynamic Emission Stokes Shift and Liquid-like Dielectric Solvation of Band Edge Carriers in Lead-Halide Perovskites. *Nat. Commun.* **2019**, *10*, 1175.
- (12) Pozzi, E. A.; Zrimsek, A. B.; Lethiec, C. M.; Schatz, G. C.; Hersam, M. C.; Van Duyne, R. P. Evaluating Single-Molecule Stokes and Anti-Stokes SERS for Nanoscale Thermometry. *J. Phys. Chem. C* **2015**, *119*, 21116–21124.

- (13) Inagaki, M.; Isogai, T.; Motobayashi, K.; Lin, K.-Q.; Ren, B.; Ikeda, K. Electronic and Vibrational Surface-Enhanced Raman Scattering: From Atomically Defined Au(111) and (100) to Roughened Au. Chemical Science 2020, 11, 9807–9817.
- (14) Kimling, J.; Maier, M.; Okenve, B.; Kotaidis, V.; Ballot, H.; Plech, A. Turkevich Method for Gold Nanoparticle Synthesis Revisited. *J. Phys. Chem. B* **2006**, *110*, 15700–15707.
- (15) Wuithschick, M.; Birnbaum, A.; Witte, S.; Sztucki, M.; Vainio, U.; Pinna, N.; Rademann, K.; Emmerling, F.; Kraehnert, R.; Polte, J. Turkevich in New Robes: Key Questions Answered for the Most Common Gold Nanoparticle Synthesis. ACS Nano 2015, 9, 7052–7071
- (16) Polte, J.; Tuaev, X.; Wuithschick, M.; Fischer, A.; Thuenemann, A. F.; Rademann, K.; Kraehnert, R.; Emmerling, F. Formation Mechanism of Colloidal Silver Nanoparticles: Analogies and Differences to the Growth of Gold Nanoparticles. *ACS Nano* **2012**, *6*, 5791–5802.
- (17) Hayes, W.; Loudon, R. Scattering of Light by Crystals; Dover Books on Physics; Courier Corporation: 2012.
- (18) Weber, W.; Merlin, R. Raman Scattering in Materials Science; Springer Series in Materials Science; Springer Berlin Heidelberg: 2000. (19) Raju, G. G. Dielectrics in Electric Fields, 2nd ed.; Taylor &
- Francis, CRC: 2016.
- (20) Fukasawa, T.; Sato, T.; Watanabe, J.; Hama, Y.; Kunz, W.; Buchner, R. Relation between Dielectric and Low-Frequency Raman Spectra of Hydrogen-Bond Liquids. *Phys. Rev. Lett.* **2005**, *95*, 197802.
- (21) Beversluis, M. R.; Bouhelier, A.; Novotny, L. Continuum Generation from Single Gold Nanostructures through Near-Field Mediated Intraband Transitions. *Phys. Rev. B* **2003**, *68*, 115433.
- (22) Mertens, J.; Kleemann, M.-E.; Chikkaraddy, R.; Narang, P.; Baumberg, J. J. How Light Is Emitted by Plasmonic Metals. *Nano Lett.* **2017**, *17*, 2568–2574.
- (23) Qin, Z.; Bischof, J. C. Thermophysical and Biological Responses of Gold Nanoparticle Laser Heating. *Chem. Soc. Rev.* **2012**, *41*, 1191–1217.
- (24) Xie, X.; Cahill, D. G. Thermometry of Plasmonic Nanostructures by Anti-Stokes Electronic Raman Scattering. *Appl. Phys. Lett.* **2016**, *109*, 183104.
- (25) Yang, H. U.; D'Archangel, J.; Sundheimer, M. L.; Tucker, E.; Boreman, G. D.; Raschke, M. B. Optical Dielectric Function of Silver. *Phys. Rev. B* **2015**, *91*, 235137.
- (26) Olmon, R. L.; Slovick, B.; Johnson, T. W.; Shelton, D.; Oh, S.-H.; Boreman, G. D.; Raschke, M. B. Optical Dielectric Function of Gold. *Phys. Rev. B* **2012**, *86*, 235147.
- (27) Hugall, J. T.; Baumberg, J. J. Demonstrating Photoluminescence from Au Is Electronic Inelastic Light Scattering of a Plasmonic Metal: The Origin of SERS Backgrounds. *Nano Lett.* **2015**, 15, 2600–2604.
- (28) Moskovits, M. Surface-Enhanced Spectroscopy. Rev. Mod. Phys. 1985, 57, 783–826.
- (29) Wei, L.; Min, W. Electronic Preresonance Stimulated Raman Scattering Microscopy. J. Phys. Chem. Lett. 2018, 9, 4294–4301.
- (30) Kuzmany, H. Solid-State Spectroscopy: An Introduction; Springer: 2009.
- (31) Doering, W. E.; Nie, S. Single-Molecule and Single-Nanoparticle SERS: Examining the Roles of Surface Active Sites and Chemical Enhancement. *J. Phys. Chem. B* **2002**, *106*, 311–317.
- (32) Shoute, L. C. T.; Bergren, A. J.; Mahmoud, A. M.; Harris, K. D.; McCreery, R. L. Optical Interference Effects in the Design of Substrates for Surface-Enhanced Raman Spectroscopy. *Appl. Spectrosc.*, AS **2009**, 63, 133–140.
- (33) Guo, Y.; Jiang, S.; Chen, X.; Mattei, M.; Dieringer, J. A.; Ciraldo, J. P.; Van Duyne, R. P. Using a Fabry—Perot Cavity to Augment the Enhancement Factor for Surface-Enhanced Raman Spectroscopy and Tip-Enhanced Raman Spectroscopy. *J. Phys. Chem. C* **2018**, *122*, 14865—14871.
- (34) Guo, Y.; Sun, D.; Ouyang, B.; Raja, A.; Song, J.; Heinz, T. F.; Brus, L. E. Probing the Dynamics of the Metallic-to-Semiconducting

Structural Phase Transformation in MoS $_2$ Crystals. Nano Lett. 2015, 15, 5081–5088.

- (35) Escobosa, A.; Sánchez-R., V. M.; Avendaño, M. A.; Navarro, G. Photoluminescence Studies of GaN: A Comparison between Layers Grown on Sapphire and Nitridated GaAs Layers. *physica status solidi* (b) **2005**, 242, 1883–1886.
- (36) Mogilevsky, R.; Nedilko, S.; Sharafutdinova, L.; Burlay, S.; Sherbatskii, V.; Boyko, V.; Mittl, S. Luminescence Study of Grown Sapphire: From Starting Material to Single Crystal. *physica status solidi c* **2009**, *6*, S179–S183.

□ Recommended by ACS

Selective Raman Enhancement with Electronic Sensitivity in Tip-Enhanced Raman Spectroscopy

Yirui Lu, Zhenglong Zhang, et al.

DECEMBER 05, 2022

THE JOURNAL OF PHYSICAL CHEMISTRY A

READ 🗹

Investigation of Interferences in Carbon Dioxide through Multidimensional Molecular-Frame High-Harmonic Spectroscopy

Daniel R. Tuthill, Louis F. DiMauro, et al.

NOVEMBER 10, 2022

THE JOURNAL OF PHYSICAL CHEMISTRY A

READ 🗹

Pressure Tuning Resonance Raman Scattering in Monolayer, Trilayer, and Many-Layer Molybdenum Disulfide

José H. Aguiar Sousa, Antonio G. Souza Filho, et al.

SEPTEMBER 27, 2022

ACS APPLIED NANO MATERIALS

READ 🗹

Critical Test of the Interaction of Surface Plasmon Resonances with Molecular Vibrational Transitions

Edward Sachet, Stefan Franzen, et al.

FEBRUARY 10, 2020

THE JOURNAL OF PHYSICAL CHEMISTRY A

READ 🗹

Get More Suggestions >